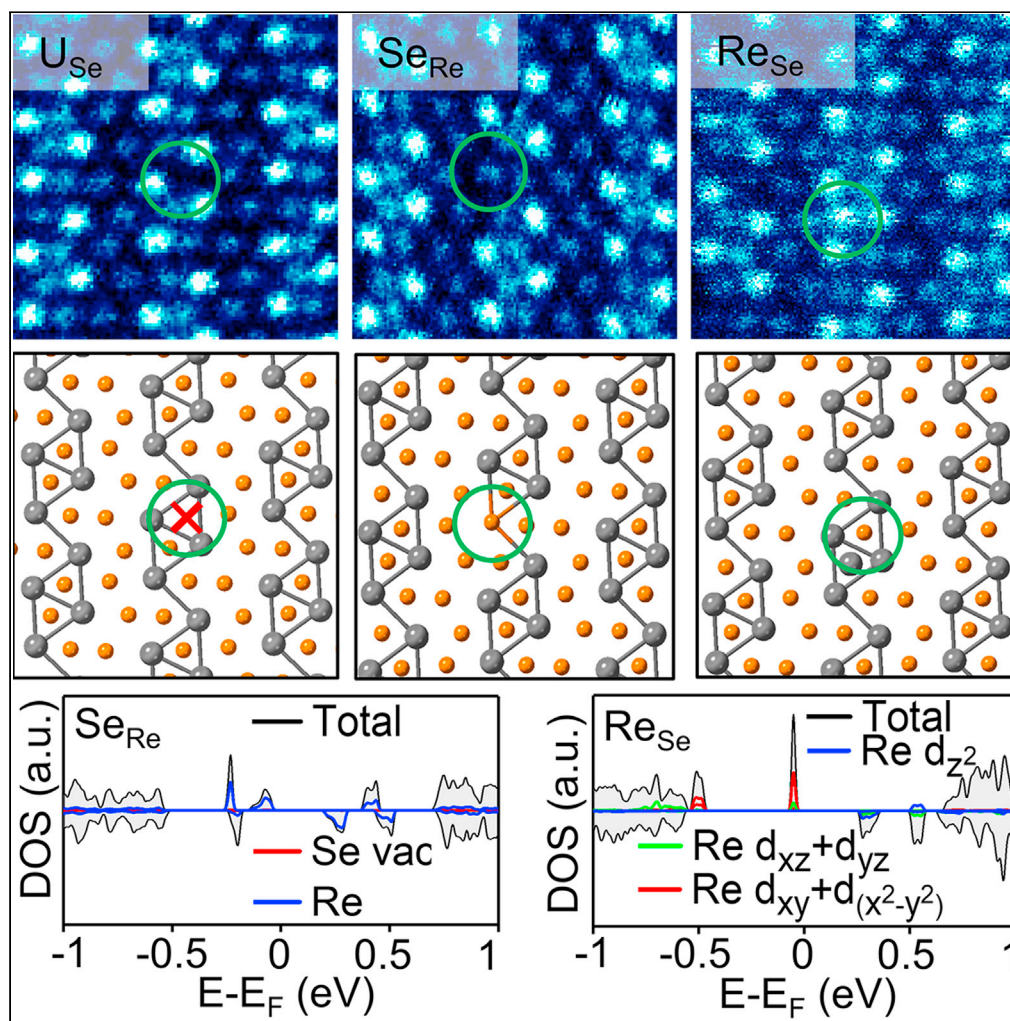## Article
Anisotropic point defects in rhenium diselenide monolayers

Yong Zhu, Lei Tao,
Xiya Chen, ...,
Shixuan Du,
Sokrates T.
Pantelides, Wu
Zhou

sxdu@iphy.ac.cn (S.D.)
wuzhou@ucas.ac.cn (W.Z.)

Highlights
Low-symmetrical ReSe$_2$ provides much more degrees of freedom for defect engineering

Isoelectronic substitution of chalcogen atoms contribute to defects recovery in ReSe$_2$

Antisite defects introduce local magnetic field in ReSe$_2$

Article

Anisotropic point defects in rhenium diselenide monolayers

Yong Zhu,[1,8] Lei Tao,[1,2,8] Xiya Chen,[1] Yinhang Ma,[1] Shoucong Ning,[3] Jiadong Zhou,[4] Xiaoxu Zhao,[4] Michel Bosman,[3] Zheng Liu,[4] Shixuan Du,[2,5,6,*] Sokrates T. Pantelides,[7] and Wu Zhou[1,5,9,*]

SUMMARY

Point defects in 1T″ anisotropic ReSe$_2$ offer many possibilities for defect engineering, which could endow this two-dimensional semiconductor with new functionalities, but have so far received limited attention. Here, we systematically investigate a full spectrum of point defects in ReSe$_2$, including vacancies (V_{Se1-4}), isoelectronic substitutions (O_{Se1-4} and S_{Se1-4}), and antisite defects (Se_{Re1-2} and Re_{Se1-4}), by atomic-scale electron microscopy imaging and density functional theory (DFT) calculations. Statistical counting reveals a diverse density of various point defects, which are further elaborated by the formation energy calculations. Se vacancy dynamics was unraveled by _in-situ_ electron beam irradiation. DFT calculations reveal that vacancies at Se sites notably introduce in-gap states, which are largely quenched upon isoelectronic substitutions (O and S), whereas antisite defects introduce localized magnetic moments. These results provide atomic-scale insight of atomic defects in 1T″-ReSe$_2$, paving the way for tuning the electronic structure of anisotropic ReSe$_2$ via defect engineering.

INTRODUCTION

Transition metal dichalcogenides (TMDs) are a focus of current research owing to their rich physics and great potential for novel technological applications(Kang et al., 2015; Keum et al., 2015; Manzeli et al., 2017; Novoselov et al., 2016; Wang et al., 2012; Yu et al., 2015). Point defects, prevailing in TMDs, influence their physical properties and thereby impact the performance of TMD-based devices. For example, sulfur vacancies in monolayer MoS$_2$ are reported to introduce localized states in the energy gap (Hong et al., 2015; Zhou et al., 2013). The concentration of sulfur vacancies is predicted to adjust the semiconductor characteristics of MoS$_2$ to vary between n-type and p-type (Yang et al., 2019a). Sulfur vacancies are also observed to drastically enhance the photoluminescence intensity in monolayer MoS$_2$ (Tongay et al., 2013). On the other hand, point defects can be intentionally introduced into TMD films to trigger new properties. In particular, the hydrogen evolution reaction performance of MoS$_2$ can be finely tuned by varying the concentration of sulfur vacancies (Wang et al., 2020; Yang et al., 2019b). Furthermore, Mo vacancies in MoS$_2$ are predicted to exhibit ferromagnetism (Koos et al., 2019). However, hexagonal TMDs with three-fold symmetry have only one type of nonequivalent chalcogen and metal sites, which limit the degree of freedom to regulate their properties via defect engineering. Additionally, previous reports about the oxidation of TMDs (Kotsakidis et al., 2019; Mirabelli et al., 2016; Sar et al., 2019) suggest the possible inclusion of oxygen impurities in the TMDs lattice. Unfortunately, it is rather challenging to reliably identify the presence of oxygen atoms in TMDs with atomic precision.

Unlike 1H- or 1T-phase TMDs, which largely exhibit isotropic properties, rhenium-based TMDs (denoted as ReX$_2$, X = S, Se) with a T″-phase structure show distinctive in-plane anisotropic properties. The T″-phase structure of ReX$_2$ can be regarded as a distorted T phase where four Re atoms undergo a 2×2 reconstruction, resulting in a cluster with a diamond-like shape (denoted as 4Re). These 4Re clusters are interconnected with each other along the **b** axis and form an overall triclinic structure (Lamfers et al., 1996; Whangbo and Canadell, 1992). This unique 2×2 superstructure contains four nonequivalent X sites and two nonequivalent Re sites in one unit cell, which are denoted as Xm (m = 1, 2, 3, 4) and Ren (n = 1, 2) exemplified by the ReSe$_2$ model shown in Figure 1D, providing more opportunities to finely tune the electronic structure of ReX$_2$. Owing to the Peierls distortion from the 1-T phase, for instance, the ReX$_2$ gives rise to a much weaker interlayer coupling. As a result, the electronic and optical properties of ReX$_2$ are largely independent of the layer thickness (Tongay et al., 2014). The anisotropic optical absorption edge of ReS$_2$ and ReSe$_2$ single
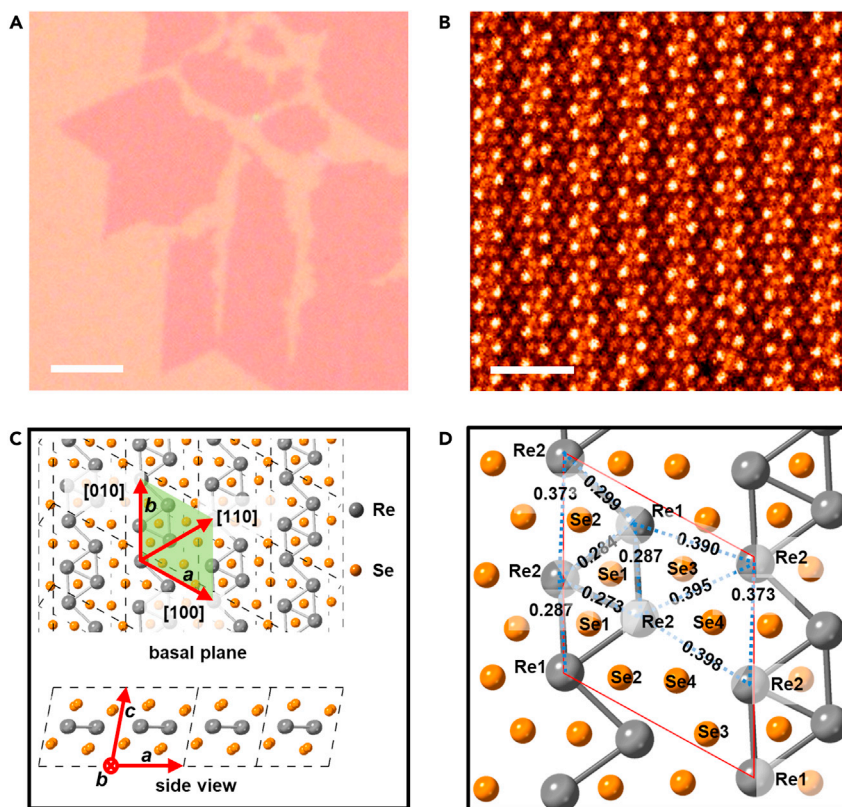
Figure 1. The morphology and crystal structure of monolayer 1T″-ReSe₂

(A) Optical image of a typical monolayer $ReSe_2$ grown by CVD on SiO_2 substrate.

(B) Atomic-resolution HAADF image of monolayer $ReSe_2$.

(C) Top view and side view along the *b* axis of the crystal model of monolayer $ReSe_2$. The gray and orange balls represent Re and Se atoms, respectively. The green-filled parallelogram covers the unit cell of monolayer $ReSe_2$.

(D) Enlarged atomic model of the unit cell marked in (C) showing the two characteristic Re sites and four Se sites. The distances between adjacent Re1 and Re2 in one unit cell are marked (in nm). Scale bars: (A) 5 μm and (B) 1 nm.

crystals are observed when linearly polarized light is perpendicularly incident to the base plane of materials(Ho et al., 1998). Although some reports have already studied point defects in $ReSe_2$ and ReS_2 (Horzum et al., 2014; Lin et al., 2015), systematic understanding of all types of point defects and the corresponding property modulations are still lacking.

In this work, by combining aberration-corrected scanning transmission electron microscopy (STEM) imaging and DFT calculations, we systematically investigate a full spectrum of point defects in monolayer $ReSe_2$. We observe both O and S substitutions at four nonequivalent Se sites (O_{Sei}, $i = 1, 2, 3, 4$; S_{Sej}, $j = 1, 2, 3, 4$), where vacancies (V_{Sek}, $k = 1, 2, 3, 4$) should have previously formed. In addition, we analyze antisite defects at two types of Re sites (Se_{Rep}, $p = 1, 2$) and antisite defects at four different Se sites (Re_{Seq}, $q = 1, 2, 3, 4$). Statistical counting results reveal that O and S atoms are prone to occupy Se1 sites, whereas vacancies tend to occur at Se4 sites, in line with the DFT calculations. Phase imaging via four-dimensional scanning transmission electron microscopy (4D-STEM), showing superior advantages in identifying light elements, is applied to unambiguously confirm the presence of isoelectronic substitutions of S and O atoms at Se sites. The measured concentrations of antisite defects, namely 0.07/nm² for Se_{Re} and 0.007/nm² for Re_{Se}, are in accordance with the trend of DFT-calculated formation energies, that is, Se_{Re} is lower in formation energy than Re_{Se}. The influence of these native point defects and several impurities on the electronic structure of monolayer $ReSe_2$ is further explored by DFT calculations. We find that vacancies in Se sites notably introduce in-gap states, whereas the in-gap states are largely quenched upon isoelectronic substitutions (O and S). Therefore, the electronic structure modifications induced by Se vacancies are healed by isoelectronic substitutional impurities, and the band structure reveals indiscernible variations compared to the pristine $ReSe_2$ monolayer. It is also

noteworthy that antisite defects at Re and Se sites induce local magnetism with values of 3 μB at Re1, Re3, and Re4 sites, and 1 μB for Re2, Se1, and Se2 sites. Charge density maps indicate that the magnetism mainly stems from the Re atoms, that is, from Re_{Se}, or from Re atoms in the vicinity of Se_{Re}.

RESULTS AND DISCUSSION

Morphology and crystal structure of monolayer 1T″-ReSe₂

Unlike conventional TMD materials in the 1-H and 1-T phases, which exhibit triangular or hexagonal morphology(Zhou et al., 2018), ReSe₂ in the 1-T″ phase shows a unique petaloid-like shape(Chen et al., 2020), as displayed in Figure 1A. Figure 1B shows an experimental STEM high-angle annular dark-field (HAADF) image of monolayer ReSe₂. Plane-view and side-view atomic models are provided in Figure 1C. The unit cell of monolayer ReSe₂ possesses lattice constants of |*a*| = 0.671 nm, |*b*| = 0.659 nm, and |*c*| = 0.672 nm (Lamfers et al., 1996). The angle between *a*[100] and *b*[010] axes is 118.9°. The lattice spacing between two adjacent 4Re diamonds in the Re-chain is 0.323 nm. The lattice spacing between two Re-chains is 0.379 nm. The Re1–Re2 bond length in the 4Re diamonds is 0.287 nm along the *b* direction and 0.284 nm along the [110] direction, respectively, as highlighted in Figure 1D. The atomic spacing differences between two adjacent 4Re diamonds from different directions are responsible for the anisotropic structural features of ReSe₂. Note that the space volumes where the four nonequivalent Se atoms are located are quite different, as reflected by the surrounding Re1-Re2 distances (see Figure 1D). Specifically, Se sites have space volumes with a descending order of Se4, Se3, Se2, and Se1 (see more details in Figure S1).

Formation energy of point defects in ReSe₂

Given the anisotropic structure of monolayer ReSe₂, we consider a full spectrum of point defects ranging from vacancies to isoelectronic substitutions, including four types of Se vacancies (V_{Se1}, V_{Se2}, V_{Se3}, and V_{Se4}), O substitution of Se atoms (O_{Se1}, O_{Se2}, O_{Se3}, and O_{Se4}), and S substitution of Se atoms (S_{Se1}, S_{Se2}, S_{Se3}, and S_{Se4}). In addition, antisite defects are considered, i.e., Se substituting Re atoms (Se_{Re1} and Se_{Re2}) and Re replacing Se atoms (Re_{Se1}, Re_{Se2}, Re_{Se3}, and Re_{Se4}). Because metal vacancies are extremely rare owing to the typical chalcogen-rich chemical vapor deposition (CVD) growth environment for TMD materials (Zhou et al., 2018), Re vacancy sites (V_{Re1} and V_{Re2}) are not discussed here. It should be stated that in this work, we employ the notation of V_{Se}, O_{Se}, S_{Se}, Re_{Se}, and Se_{Re} without specifying the exact site number to represent a collection of one category of point defects in order to simplify the discussion.

Next, we calculate the thermodynamic stability of the proposed point defects by DFT, as summarized in Figure 2 (more details in Figure S2). In Figure 2A, each characteristic Se and Re site is marked with unique colors. Overall, as shown in Figure 2B, the formation energies of O_{Se} and S_{Se} are negative (see Table S1 for detailed calculations), possessing values from −1.41 eV (Re-rich, i.e., the chemical potential μ_{Se} = −4.096 eV) to −0.64 eV (Se-rich, i.e., μ_{Se} = −3.544 eV) and from −1.322 eV (Re-rich) to −0.567 eV (Se-rich), respectively (see all values in Tables S2A and S2B). In contrast, V_{Se}, Se_{Re}, and Re_{Se} all have positive formation energies under both Se-rich and Re-rich conditions. The formation energies discussed below are all based on Se-rich conditions unless specified otherwise.

Specifically, the formation energies for vacancies at Se sites (V_{Sek}, *k* = 1, 2, 3, 4) differ by as much as 0.97 eV, with the highest at the Se1 site (2.94 eV) and the lowest at the Se4 site (2.07 eV) (see more details in Figure S2A and Table S2C). In the case of O_{Se}, the formation energy is smallest for O_{Se1} (−0.86 eV) and largest (−0.64 eV) for O_{Se3}, as can be seen in Figure 2D. In contrast, O substituting at Se2 and Se4 sites share similar formation energies (−0.71 eV for O_{Se2}, -0.72 eV for O_{Se4}), falling between those of O_{Se1} and O_{Se3} (Figure 2C). We propose that these unique site-dependent formation energy difference of O impurities stems from their different local chemical bonding environments at each Se site. The spacing volume between adjacent 4Re along the [110] direction is larger than the interspace within 4Re (see Figures 1D and S1B) so that O atoms with much smaller atomic radius compared with Re and Se atoms would preferentially occupy the Se1 site owing to the reduced bond lengths (0.208 nm). Similarly, a higher formation energy of O_{Se3} may be attributed to longer bond lengths (0.216 nm) between the O atom and its surrounding Re atoms, leading to O_{Se3} being relatively less stable. The formation energy trend of substitutional S at Se sites is similar to that of O substitution (Figures 2C and 2D). Nonetheless, the relative tendency of the formation energies for O and S substitution at Se2 and Se4 sites is opposite with minor difference, that is, S_{Se2} (−0.65 eV) slightly lower than S_{Se4} (−0.61 eV). With regard to vacancies at Se sites, reasoning along the same lines explains the lower formation energies for V_{Se3} and V_{Se4} owing to the larger space volumes at Se3 and Se4 sites.
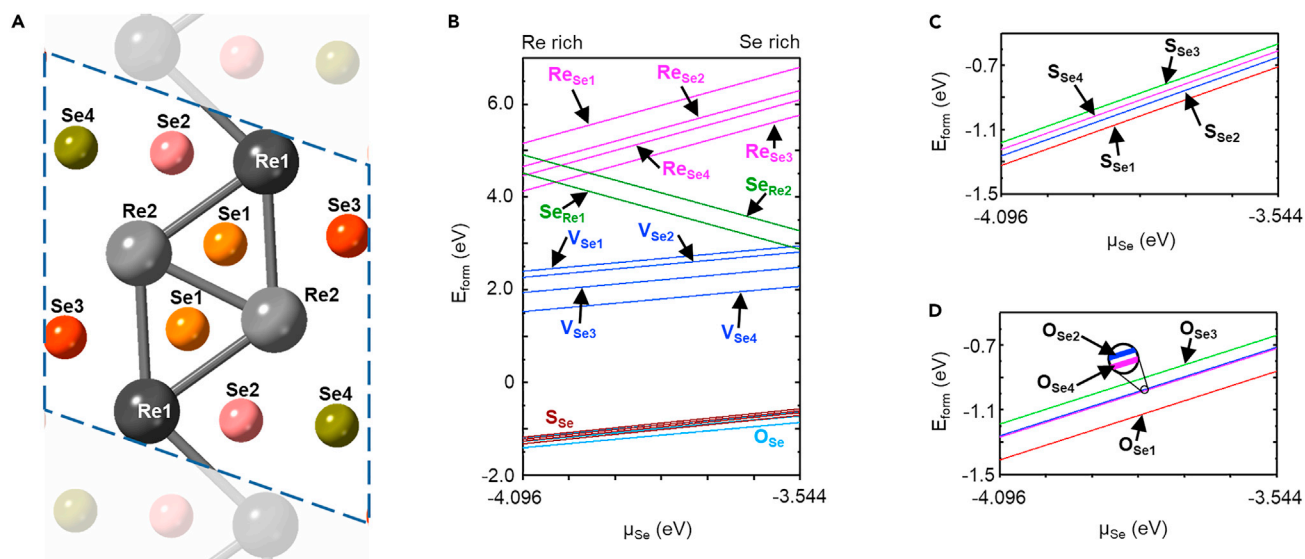
Figure 2. Formation energies of point defects in ReSe₂ monolayers

(A) The atomic model of four characteristic Se sites (Se1, Se2, Se3, and Se4) and two unique Re sites (Re1 and Re2) marked with different colored balls in one unit cell.

(B) Formation energy curves of various point defects in the ReSe$_2$ monolayer as a function of Se chemical potential. Each curve represents one type of point defect.

(C) Enlarged formation energy curves of S$_{Se}$ at four nonequivalent Se sites.

(D) Enlarged formation energy curves of O$_{Se}$ at four nonequivalent Se sites.

The formation energies of antisite defects were also calculated, and they are much higher than those of vacancies or isoelectronic substitutions at Se sites (Figure 2B). In the case of Re$_{Se}$, Re$_{Se4}$ (6.1 eV) and Re$_{Se3}$ (5.8 eV) are energetically more favorable than Re$_{Se2}$ (6.3 eV) and Re$_{Se1}$ (6.8 eV) (Figure S2C). As a Re atom has a much larger atomic radius than a Se atom, the available spacing is the key factor that determines the thermodynamic stability of Re$_{Se}$ antisites. Because the space volume at Se3 and Se4 sites is much larger than that at Se1 and Se2 sites (see Figure S1B), Re atoms show a tendency to occupy the Se3 and Se4 positions. Comparatively, Se$_{Re}$ shows a lower formation energy than Re$_{Se}$ (Figure 2B). Se$_{Re1}$ (2.87 eV) with lower formation energy than Se$_{Re2}$ (3.29 eV) likewise reflects the nonequivalence of two Re sites.

Statistics of primary point defects in ReSe₂

In order to verify the relative formation energy trend of these point defects, we carried out statistical defect counting in a monolayer ReSe$_2$ sample grown by CVD under Se-rich conditions (see STAR Methods for details about the sample growth). A large number of atomic-resolution STEM-HAADF images were acquired for point defect statistical analysis. However, the Z-contrast in STEM-HAADF images, that is, $I \sim Z^{1.33 \sim 2.0}$ (I is the image intensity and Z is the atomic number) (Nellist and Pennycook, 2000; Pennycook and Boatner, 1988; Pennycook and Jesson, 1990; Treacy, 2011), results in a situation that possible signal from the light O and S atoms would be easily overwhelmed by the strong signal from the heavy Se and Re atoms. Although STEM medium-angle annular dark-field (MAADF) imaging can slightly enhance the contrast of light elements, it is still difficult to identify O atoms in monolayer ReSe$_2$. Given these conditions, we may consider using electron energy loss (EEL) spectroscopy to discern the light elements, but this is challenging here as well. A good signal-to-noise ratio (SNR) EEL spectrum normally requires a much longer acquiring time (about several hundred milliseconds) than HAADF imaging (about several tens of microseconds per pixel). Hence, before generating a satisfactory atomically resolved EEL spectrum, beam-sensitive ReSe$_2$ monolayers would be severely damaged by the impact of the electron beam. Therefore, we use the sign of "U$_{Se}$" to temporarily denote the Se sites with much lower HAADF contrast and the capital "U" stands for undetermined (i.e., the exact identity to be determined). The second step is to determine the density of each point defect in monolayer ReSe$_2$ by an atom-by-atom site location through the center of mass method (Gong et al., 2014; Krivanek et al., 2010). A demonstration of the process is shown in Figure S3.
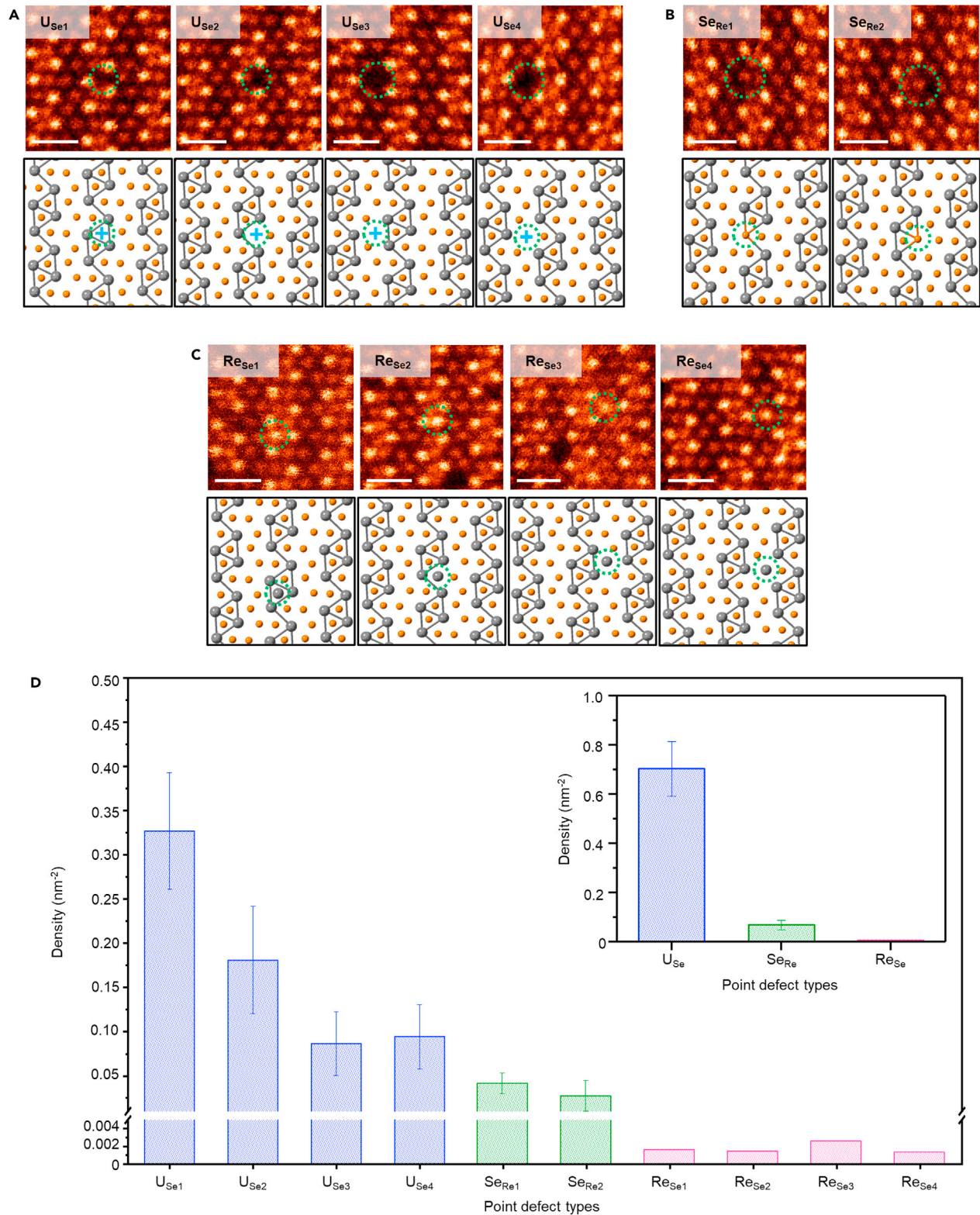
Figure 3. Main types of point defects and their densities in monolayer ReSe$_2$

(A) STEM-HAADF images of four types of U$_{Se}$ in monolayer ReSe$_2$. The capital letter U means the exact identity remains to be determined.

(B) Antisite defects with Se substitution in Re sites.

Figure 3. *Continued*

(C) Antisite defects with Re substitution in Se sites.

(D) Statistics of major point defects. In (A)–(C), the upper half shows the experimental images of specific point defects while the corresponding structure models are depicted in the lower panels. These point defects, i.e., U_{Se}, Se_{Re}, and Re_{Se}, are marked with green dashed circles in the HAADF images and the corresponding models, respectively. U_{Se} point defects are marked with light blue cross signs in the corresponding structure models. The inset histogram in (D) sums the same type of point defects in Se or Re sites. Point defects in Se sites dominate in $ReSe_2$. The total area size for statistical analysis is about 2500 nm^2. Scale bars in (A–C): 0.5 nm. Error bars in (D): 0.11/nm^2 for U_{Se}, 0.019/nm^2 for Se_{Re}, 0.066/nm^2 for U_{Se1}, 0.061/nm^2 for U_{Se2}, 0.036/nm^2 for U_{Se3}, 0.036/nm^2 for U_{Se4}, 0.011/nm^2 for Se_{Re1}, 0.017/nm^2 for Se_{Re2}.

Figure 3 presents the point defects observed in STEM-HAADF imaging (see plenty of point defects in a large field of view shown in Figure S4), and the densities of point defects are summarized in the histogram, including the four U_{Se} point defects at Se sites (Figure 3A), two antisite defects at Re sites (Figure 3B), and four antisite defects at Se sites (Figure 3C). As Figure 3D shows, in general, U_{Se} dominates in the $ReSe_2$ monolayer with a concentration of ∼0.7/nm^2, which is higher than that in CVD-grown MoS_2 with a concentration of the dominant vacancies of about 0.14/nm^2 (Hong et al., 2015). Furthermore, the concentrations of point defects with dim image contrast vary significantly at the four different Se sites and exhibit a trend similar to that of the relative formation energies of four S_{Se} (see Figure 2C) and four O_{Se} (see Figure 2D, if we neglect the 0.01 eV difference between O_{Se4} and O_{Se2}). More experimental evidence is required in order to identify the U_{Se} as S_{Se} or O_{Se}, as will be discussed in the latter section.

The presence of antisite defects at Se and Re sites (Figures 3B and 3C) can be readily verified by the STEM-HAADF images (see Figure S4B). The concentrations of Re_{Se} and Se_{Re} (see Figure 3D) are site-dependent and match well with the formation energy trends. The total concentration of Se_{Re} (about 0.07/nm^2) is much lower than U_{Se} (about 0.7/nm^2). Because of a much higher formation energy (more than 5.7 eV) and the Se-rich growth environment, the concentration of Re_{Se} (0.007/nm^2) is one order of magnitude lower than U_{Se} and Se_{Re}.

4D-STEM identification of O and S atoms in $ReSe_2$

In order to determine the possible presence of O or S atoms at the "U_{Se}" sites, we conducted 4D-STEM experiments. Via phase imaging reconstruction, 4D-STEM is able to greatly enhance the contrast of light atoms surrounded by heavy atoms. Meanwhile, with the aid of a high-performance camera, 4D-STEM imaging could significantly reduce the data acquisition time down to several milliseconds, which greatly minimizes the damage to the sample. We first carry out 4D-STEM phase image simulations on a monolayer $ReSe_2$ containing three types of defects, that is, V_{Se}, O_{Se}, and S_{Se} (Figures 4A and 4B). Compared with STEM-HAADF imaging, the reconstructed phase image using the single-side band (SSB) method (See STAR Methods for more details) enhances the contrast of O or S atoms by three to five times (see Figure S5 and Table S3 for more details), making it possible to differentiate O and S atoms from "U_{Se}" defects.

The experimental 4D-STEM results are displayed in Figures 4C and 4D. According to the simultaneously acquired HAADF image shown in Figure 4D, two patches (number 1# and 2#) containing defects in Figure 4C are selected for analysis. The intensity line profile analysis shown in Figure 4E suggests that the dim contrast at Se sites in the STEM-HAADF image is due to S (at 1# position) atoms and O (at 2# position) atoms, respectively. These results indicate that via 4D-STEM imaging, S and O atoms can be distinguished even in TMD materials such as $ReSe_2$.

Generation of Se vacancies under electron beam irradiation

The dynamical evolution of the various defects in $ReSe_2$ monolayer under electron irradiation was also surveyed to exam the reliability of the formation energies for vacancies at Se sites. Because the $ReSe_2$ monolayer is highly sensitive to electron beam irradiation, the probe current was reduced significantly in order to realize a better control of defect propagation (see STAR Methods for more details). We carefully controlled the electron dose so that only vacancies at chalcogen sites could be generated. Figures 5A–5D show sequential images of the vacancies generated by the electron beam. As the electron dose gradually increases from 0.7×10^6 $e^- \bullet nm^{-2}$ to 2.1×10^6 $e^- \bullet nm^{-2}$, as shown in Figure 5E, the density of total vacancies at each Se site rises subsequently except V_{Se1}. The decline of V_{Se1} was probably due to the refilling by mobile Se adatoms. More importantly, the ratio of vacancy concentrations at Se4 sites (marked with green circles in Figures 5A–5D) over the total vacancies at Se sites becomes larger, from 48% to 66%, as shown in Figure 5F. This trend further corroborates the smallest formation energy of V_{Se4} among four V_{Se}, as displayed
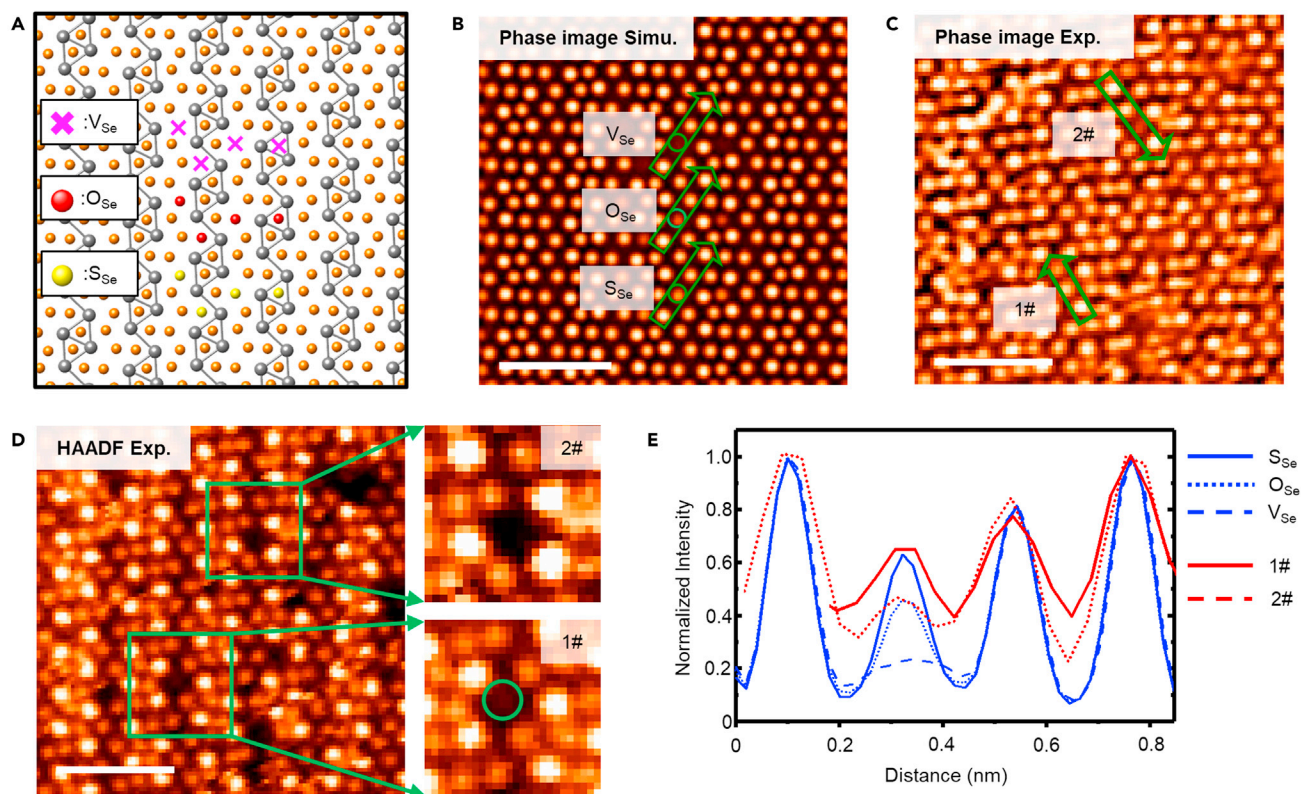
Figure 4. 4D-STEM phase image analysis of point defects in 1T″-ReSe₂ monolayer

(A) Monolayer $ReSe_2$ crystal model with three types of point defects: vacancy (marked with magenta cross sign), O (red ball), and S (yellow ball) atoms at different Se sites.

(B) 4D-STEM phase image simulation using the crystal model in (A).

(C) Phase reconstructed image of a typical region using the SSB method.

(D) Simultaneously acquired STEM-HAADF image of the same region in (C) where the 4D-STEM data were acquired.

(E) Intensity comparison of the point defects between simulated and experimental 4D-STEM phase images. The blue soild curve, dot curve, and dashed curve represent line profiles across S_{Se}, O_{Se}, and V_{Se} in (B), respectively; the red solid and dashed curves are the intensity line profiles across different point defects in (C). The line profiles show that the dark contrast at the Se sites in the HAADF images are either S atoms or O atoms. Scale bars: 1 nm.

in Figure S2A and Table S2C. The disagreement between the concentration ratios of V_{Se2} and V_{Se3} with their relative formation energies is likely caused by the dynamic effects such as the moving of the vacancies.

DFT calculations also show that in general the total energy of the monolayer $ReSe_2$ only increases slightly (less than 0.1 eV/nm²) with the increasing concentration of Se vacancies (see Figure S6), with the exception of V_{Se4}, where the total energy decreases by 0.28 eV/nm² when the concentration of V_{Se4} increases from 0.16/nm² to 0.64/nm². Note that at all V_{Se} concentrations considered in our calculations, the total energy is consistently lower for cases of V_{Se3} and V_{Se4} than that for V_{Se1} and V_{Se2} by ~ 0.3 eV. In addition, the overall Re-chain structure of the $ReSe_2$ monolayer and the anisotropy remain unchanged at a relatively high concentration of Se vacancies as shown in Figure S7. These results indicate that vacancies at Se3 and Se4 sites are easier to form as compared with those at Se1 and Se2 sites. Our calculations are in line with previous experimental results reported by Lin et al. that Se atoms at Se3 and Se4 sites are preferentially knocked out under high electron dose irradiation (Lin et al., 2015).

Electronic structure of ReSe₂ with point defects

Finally, the effects of the observed point defects on the electronic structure of $ReSe_2$ monolayer are studied. We calculated the density of states (DOS) of all types of point defects mentioned above. Figure 6 lists the representative DOS in each type of point defect, that is, the DOS of V_{Se1}, S_{Se1}, O_{Se1}, Se_{Re1}, and Re_{Se1} (see Figures S9 and S10 for all DOS results). As the density of Se vacancies increases, additional defect states near the Fermi level appear (Figure 6B), similar to previous DFT calculations on defect states in monolayer
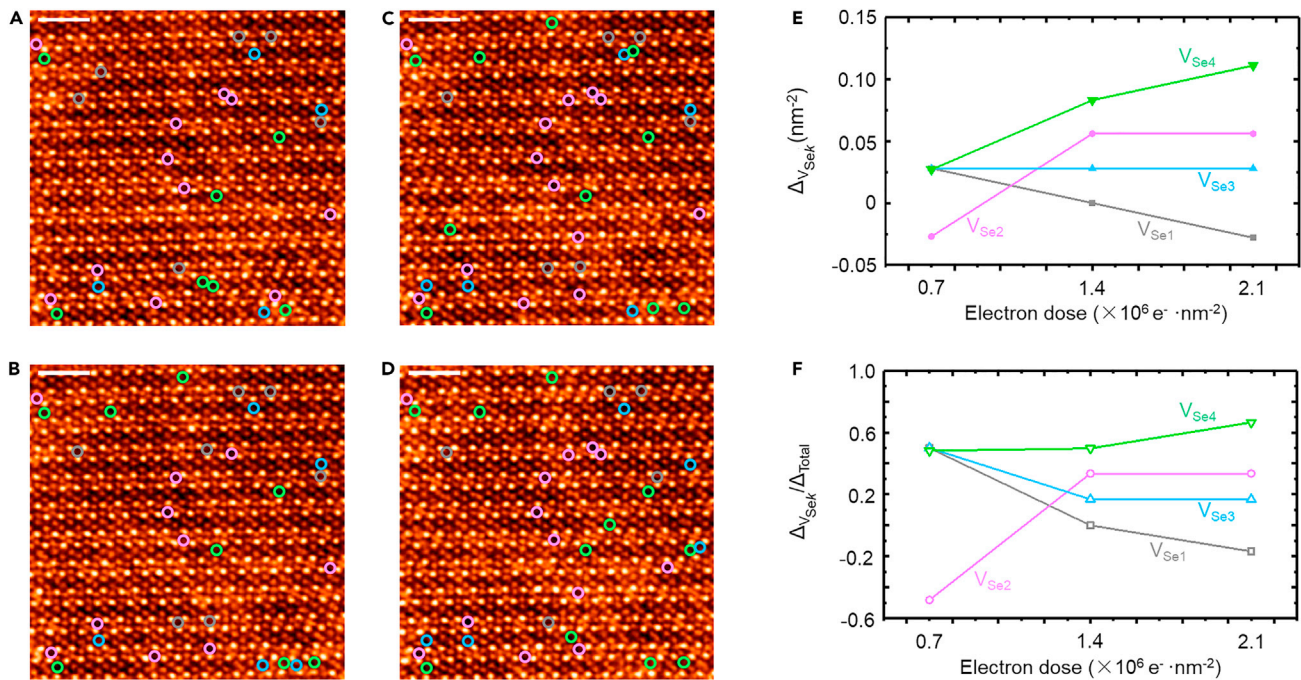
Figure 5. Se vacancies generated by electron beam irradiation

(A–D) Upon prolonged e-beam irradiation, an increasing number of vacancies are created at Se sites in ReSe$_2$ monolayer, as labeled with gray circles (vacancies at Se1 sites), light purple circles (vacancies at Se2 sites), light blue circles (vacancies at Se3 sites), and green circles (vacancies at Se4 sites).

(E) The increment of vacancy concentration ($\Delta_{vacancy}$) at each Se site in (B–D) when compared with (A).

(F) The ratio of each vacancy-concentration increment ($V_{Se}k_{=1-4}/\Delta_{Total}$) at Se sites in (B–D) when compared with (A). Scale bars: 1 nm.

MoS$_2$ (Yang et al., 2019a). The calculated DOS of ReSe$_2$ with S and O substitutions at Se sites (Figures 6C and 6D) reveals that the density of states near the Fermi level remains almost the same as in the pristine ReSe$_2$ (Figure 6A) after isoelectronic doping. This phenomenon is consistent with the observation by Tang et al. that oxygen dopants in the form of substitution of chalcogen atoms could reduce the bandgap of intrinsic MoS$_2$ without introducing in-gap states and greatly improve its carrier mobility(Tang et al., 2020). In ReSe$_2$, only a small energy barrier of ∼84 meV needs to be overcome to allow external O$_2$ molecules to dissociate when a O$_2$ molecule is adsorbed at a Se vacancy, as shown in Figure S8, suggesting that Se vacancies in monolayer ReSe$_2$ facilitate the dissociation of O$_2$ molecules and subsequently are filled by dissociated O atoms. In light of a usual aging process(Gao et al., 2016; Kotsakidis et al., 2019; Sar et al., 2019) and vacancy-induced oxidation(Liu et al., 2015) in TMD materials, we may expect that slight aging of ReSe$_2$ in ambient conditions would not significantly degrade the in-plane anisotropy and the transport properties.

In the case of antisite defects, the DOS is very different from that of vacancies or O(S) substitutions at Se sites. Because of the unpaired electrons, the antisite defects of Re$_{Se}$ and Se$_{Re}$ introduce magnetic moments into the ReSe$_2$ lattice. Specifically, the total magnetic moment of the ground state of one Re atom is 3 μ_B at Re$_{Se1}$, 1 μ_B at Re$_{Se2}$, 3 μ_B at Re$_{Se3}$, and 3 μ_B at Re$_{Se4}$ antisites, respectively. For antisite defects at Re sites, the calculated magnetic moment is 1 μ_B in both Se$_{Re1}$ and Se$_{Re2}$. To further identify the origin of magnetism, the spin-resolved charge density is calculated, and the representative ones are shown in Figures 6G–6J (see Figure S10 for all the six antisite results). Figure 6I (top view) and 6J (side view) show that, in the case of Re$_{Se1}$, the spin-polarized electrons are mainly localized on the Re atom. In the case of Se$_{Re1}$ as shown in Figure 6G (top view) and Figure 6H (side view), the magnetism of Se$_{Re}$ is mainly contributed by the nearby Re atoms. In pristine ReSe$_2$, the conduction band is composed primarily of the Re d-orbitals. Owing to the substitutional Se atom in Se$_{Re1}$, the d-orbitals split, and subsequently the spin-polarized electrons are localized on the Re atoms nearby. The coordination geometry of the Re is octahedral in Re$_{Se2}$ while tetrahedral in Re$_{Se1}$, Re$_{Se3}$, and Re$_{Se4}$, resulting in the split e_g and t_{2g} orbitals in Re$_{Se1}$, Re$_{Se3}$, and Re$_{Se4}$, and consequently higher magnetic moments than that in Re$_{Se2}$. In light of the magnetic moment differences between antisite defects at Sem (m = 1, 2, 3, 4) sites and Rem (m = 1, 2) sites, we may envision building an anisotropically controllable solid-state spin qubit system
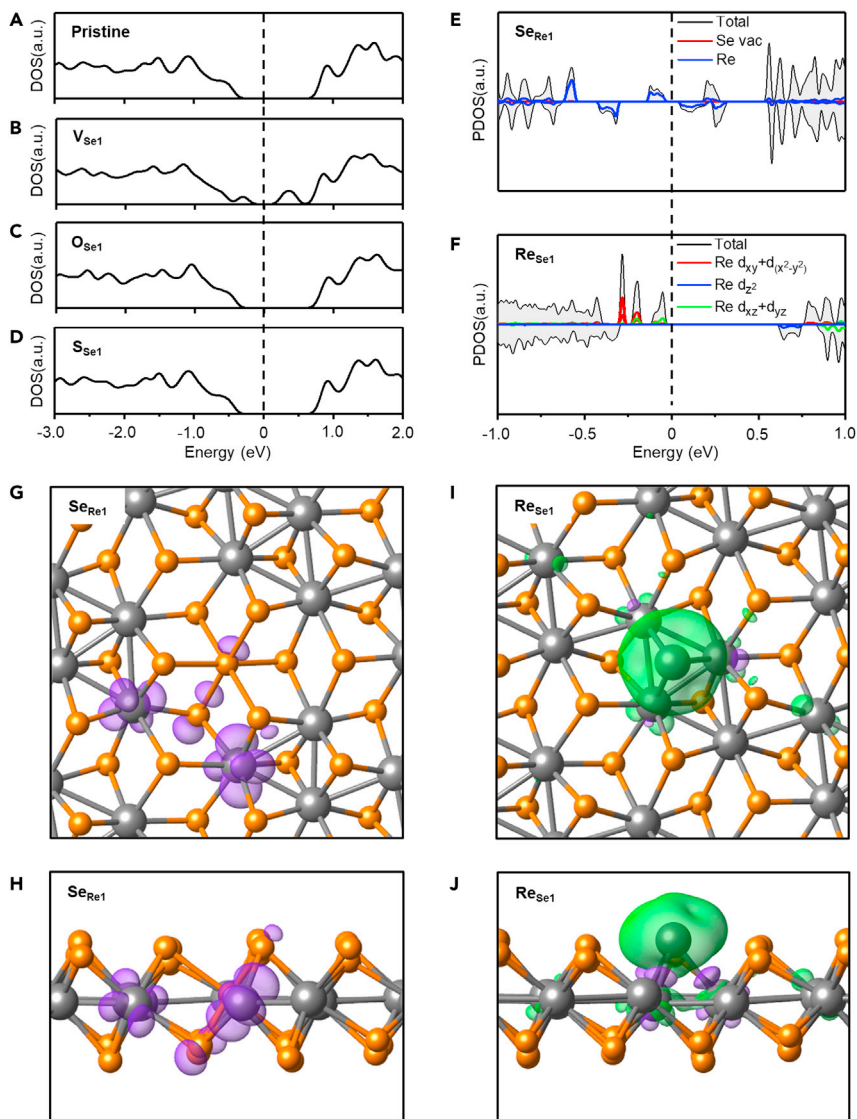
Figure 6. Calculated electronic structures of monolayer ReSe₂ with different point defects

(A–D) The DOS of pristine ReSe$_2$ monolayer and ReSe$_2$ monolayer with point defects of V_{Se1}, O_{Se1}, and S_{Se1} at Se1 sites. There are states in the energy gap in the case of V_{Se1}.

(E) The DOS of ReSe$_2$ when one Re1 site atom is substituted by a Se atom (Se_{Re1}).

(F) The DOS of ReSe$_2$ when one Se1 site atom is substituted by a Re atom (Re_{Se1}). The black curves in (E) and (F) represent the total DOS of the point defects. The dashed vertical lines in (A–F) mark Fermi level.

(G and H) Top view (G) and side view (H) of the spin-resolved charge density of ReSe$_2$ with Se_{Re1} showing the spin-polarized electrons mainly located on Re atoms near Se atoms.

(I and J) Top view (I) and side view (J) of the spin-resolved charge density of ReSe$_2$ with Re_{Se1} showing the spin-polarized electrons mainly located on Re atoms. Green (purple) colors represent spin up (down) electrons. Magnetic moment is introduced into ReSe$_2$ in both types of antisite defects and mainly arises from the Re atoms.

utilizing ReSe$_2$(Tsai et al., 2021). Alteration of local magnetism of these materials may be realized through changing the density of antisite defects in a ReSe$_2$ film by controlling the growth parameters.

Conclusions

In summary, we systematically investigate point defects with anisotropic distributions in monolayer 1T′′-ReSe$_2$ and their electronic structures through first-principles calculations and STEM imaging. Because of the anisotropic structure of ReSe$_2$, there are four types of nonequivalent Se sites and two types of

nonequivalent Re sites in one unit cell. We find that point defects at Se sites dominate in pristine monolayer $ReSe_2$, followed by antisite defects Se_{Re} and Re_{Se}, that is, $0.7/nm^2$ for point defects at Se sites, $0.07/nm^2$ for Se_{Re}, and $0.007/nm^2$ for Re_{Se}. Isoelectronic substitutions of O and S atoms at Se sites are preferentially formed within the Re-chains, while Se vacancies tend to appear in the channels between Re-chains. DFT calculations reveal that Se vacancies result in in-gap states, whereas isoelectronic substitution of O and S atoms at Se sites hardly change the band structure near the Fermi level. Moreover, antisite defects of Re_{Se} introduce large site-dependent magnetic moments into this system while Se_{Re} antisite defects induce relatively weak magnetic moments independent of the anisotropy. These results show that the anisotropic structure of 1T''-$ReSe_2$ offers extra degrees of freedom to finely tune the physical properties via defect engineering. The often-neglected isoelectronic substitution at chalcogen sites provides an alternative approach to recovering the intrinsic properties of defective 2D materials.

Limitations of the study

Oxygen atoms are commonly present in TMD materials especially in the ambient environment. Although 4D-STEM imaging distinguishes the oxygen atoms in $ReSe_2$, statistical defect analysis via high-throughput 4D-STEM experiment remains challenging, especially for electron-beam sensitive 2D materials.

STAR★METHODS

Detailed methods are provided in the online version of this paper and include the following:

- KEY RESOURCES TABLE
- RESOURCE AVAILABILITY
  - Lead contact
  - Materials availability
  - Date and code availability
- EXPERIMENTAL MODEL AND SUBJECT DETAILS
- METHOD DETAILS
  - $ReSe_2$ growth and TEM sample preparation
  - Electron microscopy characterization
  - Density functional calculations
- QUANTIFICATION AND STATISTICAL ANALYSIS

AUTHOR CONTRIBUTIONS

W. Zhou and S.X. Du conceived and supervised the project. J.D. Zhou and Z. Liu provided the sample. Y. Zhu and X.Y. Chen designed and conducted the STEM experiments. L. Tao conducted the DFT calculations. Y. Zhu, Y.H. Ma, and S.C Ning analyzed the 4D-STEM data. Y. Zhu and L. Tao wrote the paper. X.X. Zhao, M. Bosman, and S.T. Pantelides contributed to the revision of the paper. All authors discussed the results and commented on the manuscript.

DECLARATION OF INTERESTS

The authors declare no competing interests.

REFERENCES

Barthel, J. (2018). Dr. Probe: a software for high-resolution STEM image simulation. Ultramicroscopy 193, 1–11. https://doi.org/10.1016/j.ultramic.2018.06.003.

Blochl, P.E. (1994). Projector augmented-wave method. Phys. Rev. B 50, 17953–17979. https://doi.org/10.1103/PhysRevB.50.17953.

Chen, X.Y., Lei, B., Zhu, Y., Zhou, J.D., Liu, Z., Ji, W., and Zhou, W. (2020). Pristine edge structures of T ''-phase transition metal dichalcogenides (ReSe₂, ReS₂) atomic layers. Nanoscale 12, 17005–17012. https://doi.org/10.1039/d0nr03530k.

Du, H. (2015). A nonlinear filtering algorithm for denoising HR(S)TEM micrographs. Ultramicroscopy 151, 62–67. https://doi.org/10.1016/j.ultramic.2014.11.012.

Gao, J., Li, B.C., Tan, J.W., Chow, P., Lu, T.M., and Koratkar, N. (2016). Aging of transition metal dichalcogenide monolayers. ACS Nano 10, 2628–2635. https://doi.org/10.1021/acsnano.5b07677.

Gong, Y.J., Liu, Z., Lupini, A.R., Shi, G., Lin, J.H., Najmaei, S., Lin, Z., Elias, A.L., Berkdemir, A., You, G., et al. (2014). Band gap engineering and layer-by-layer mapping of selenium-doped molybdenum disulfide. Nano Lett. 14, 442–449. https://doi.org/10.1021/nl4032296.

Ho, C.H., Huang, Y.S., Tiong, K.K., and Liao, P.C. (1998). Absorption-edge anisotropy in ReS₂ and ReSe₂ layered semiconductors. Phys. Rev. B 58, 16130–16135. https://doi.org/10.1103/PhysRevB.58.16130.

Hong, J., Hu, Z., Probert, M., Li, K., Lv, D., Yang, X., Gu, L., Mao, N., Feng, Q., Xie, L., et al. (2015). Exploring atomic defects in molybdenum disulphide monolayers. Nat. Commun. 6, 6293–6301. https://doi.org/10.1038/ncomms7293.

Horzum, S., Cakir, D., Suh, J., Tongay, S., Huang, Y.S., Ho, C.H., Wu, J., Sahin, H., and Peeters, F.M. (2014). Formation and stability of point defects in monolayer rhenium disulfide. Phys. Rev. B 89, 155433–155440. https://doi.org/10.1103/PhysRevB.89.155433.

Kang, K., Xie, S.E., Huang, L.J., Han, Y.M., Huang, P.Y., Mak, K.F., Kim, C.J., Muller, D., and Park, J. (2015). High-mobility three-atom-thick semiconducting films with wafer-scale homogeneity. Nature 520, 656–660. https://doi.org/10.1038/nature14417.

Keum, D.H., Cho, S., Kim, J.H., Choe, D.H., Sung, H.J., Kan, M., Kang, H., Hwang, J.Y., Kim, S.W., Yang, H., et al. (2015). Bandgap opening in few-layered monoclinic MoTe₂. Nat. Phys. 11, 482–487. https://doi.org/10.1038/nphys3314.

Koos, A.A., Vancso, P., Szendro, M., Dobrik, G., Silva, D.A., Popov, Z.I., Sorokin, P.B., Henrard, L., Hwang, C., Biro, L.P., and Tapaszto, L. (2019). Influence of native defects on the electronic and magnetic properties of CVD grown MoSe₂ single layers. J. Phys. Chem. C 123, 24855–24864. https://doi.org/10.1021/acs.jpcc.9b05921.

Kotsakidis, J.C., Zhang, Q.H., de Parga, A.L.V., Currie, M., Helmerson, K., Gaskill, D.K., and Fuhrer, M.S. (2019). Oxidation of monolayer WS₂ in ambient is a photoinduced process. Nano Lett.

19, 5205–5215. https://doi.org/10.1021/acs.nanolett.9b01599.

Kresse, G., and Furthmuller, J. (1996). Efficient iterative schemes for ab initio total-energy calculations using a plane-wave basis set. Phys. Rev. B 54, 11169–11186. https://doi.org/10.1103/PhysRevB.54.11169.

Krivanek, O.L., Chisholm, M.F., Nicolosi, V., Pennycook, T.J., Corbin, G.J., Dellby, N., Murfitt, M.F., Own, C.S., Szilagyi, Z.S., Oxley, M.P., et al. (2010). Atom-by-atom structural and chemical analysis by annular dark-field electron microscopy. Nature 464, 571–574. https://doi.org/10.1038/nature08879.

Lamfers, H.J., Meetsma, A., Wiegers, G.A., and deBoer, J.L. (1996). The crystal structure of some rhenium and technetium dichalcogenides. J. Alloys Compounds 241, 34–39. https://doi.org/10.1016/0925-8388(96)02313-4.

Lin, Y.-C., Komsa, H.-P., Yeh, C.-H., Bjorkman, T., Liang, Z.-Y., Ho, C.-H., Huang, Y.-S., Chiu, P.-W., Krasheninnikov, A.V., and Suenaga, K. (2015). Single-layer ReS₂: two-dimensional semiconductor with tunable in-plane anisotropy. ACS Nano 9, 11249–11257. https://doi.org/10.1021/acsnano.5b04851.

Liu, H., Han, N., and Zhao, J. (2015). Atomistic insight into the oxidation of monolayer transition metal dichalcogenides: from structures to electronic properties. RSC Adv. 5, 17572–17581. https://doi.org/10.1039/c4ra17320a.

Manzeli, S., Ovchinnikov, D., Pasquier, D., Yazyev, O.V., and Kis, A. (2017). 2D transition metal dichalcogenides. Nat. Rev. Mater. 2, 17033–17048. https://doi.org/10.1038/natrevmats.2017.33.

Mirabelli, G., McGeough, C., Schmidt, M., McCarthy, E.K., Monaghan, S., Povey, I.M., McCarthy, M., Gity, F., Nagle, R., Hughes, G., et al. (2016). Air sensitivity of MoS₂, MoSe₂, MoTe₂, HfS₂, and HfSe₂. J. Appl. Phys. 120, 12512–12521. https://doi.org/10.1063/1.4963290.

Nellist, P.D., and Pennycook, S.J. (2000). The principles and interpretation of annular dark-field Z-contrast imaging. Adv. Imaging Electron Phys. 113, 147–203. https://doi.org/10.1016/s1076-5670(00)80013-0.

Novoselov, K.S., Mishchenko, A., Carvalho, A., and Neto, A.H.C. (2016). 2D materials and van der Waals heterostructures. Science 353, 461–473. https://doi.org/10.1126/science.aac9439.

Pennycook, S.J., and Boatner, L.A. (1988). Chemically sensitive structure-imaging with a scanning transmission electron microscope. Nature 336, 565–567. https://doi.org/10.1038/336565a0.

Pennycook, S.J., and Jesson, D.E. (1990). High-resolution incoherent imaging of crystals. Phys. Rev. Lett. 64, 938–941. https://doi.org/10.1103/PhysRevLett.64.938.

Pennycook, T.J., Lupini, A.R., Yang, H., Murfitt, M.F., Jones, L., and Nellist, P.D. (2015). Efficient phase contrast imaging in STEM using a pixelated detector. part 1: experimental demonstration at atomic resolution.

Ultramicroscopy 151, 160–167. https://doi.org/10.1016/j.ultramic.2014.09.013.

Perdew, J.P., Burke, K., and Ernzerhof, M. (1996). Generalized gradient approximation made simple. Phys. Rev. Lett. 77, 3865–3868. https://doi.org/10.1103/PhysRevLett.77.3865.

Rodenburg, J.M., McCallum, B.C., and Nellist, P.D. (1993). Experimental tests on double-resolution coherent imaging via STEM. Ultramicroscopy 48, 304–314. https://doi.org/10.1016/0304-3991(93)90105-7.

Sar, H., Ozden, A., Demiroglu, I., Sevik, C., Perkgoz, N.K., and Ay, F. (2019). Long-term stability control of CVD-grown monolayer MoS₂. Phys. Status Solidi Rapid Res. Lett. 13, 1800687–1800694. https://doi.org/10.1002/pssr.201800687.

Savitzky, B.H., Zeltmann, S.E., Hughes, L.A., Brown, H.G., Zhao, S.T., Pelz, P.M., Pekin, T.C., Barnard, E.S., Donohue, J., DaCosta, L.R., et al. (2021). py4DSTEM: a software package for four-dimensional scanning transmission electron microscopy data analysis. Microsc. Microanal. 27, 712–743. https://doi.org/10.1017/s1431927621000477.

Tang, J., Wei, Z., Wang, Q.Q., Wang, Y., Han, B., Li, X.M., Huang, B.Y., Liao, M.Z., Liu, J.Y., Li, N., et al. (2020). In situ oxygen doping of monolayer MoS₂ for novel electronics. Small 16, 2004276–2004284. https://doi.org/10.1002/smll.202004276.

Tongay, S., Sahin, H., Ko, C., Luce, A., Fan, W., Liu, K., Zhou, J., Huang, Y.S., Ho, C.H., Yan, J.Y., et al. (2014). Monolayer behaviour in bulk ReS₂ due to electronic and vibrational decoupling. Nat. Commun. 5, 3252–3258. https://doi.org/10.1038/ncomms4252.

Tongay, S., Suh, J., Ataca, C., Fan, W., Luce, A., Kang, J.S., Liu, J., Ko, C., Raghunathanan, R., Zhou, J., et al. (2013). Defects activated photoluminescence in two-dimensional semiconductors: interplay between bound, charged, and free excitons. Sci. Rep. 3, 2657–2662. https://doi.org/10.1038/srep02657.

Treacy, M.M.J. (2011). Z dependence of electron scattering by single atoms into annular dark-field detectors. Microsc. Microanal. 17, 847–858. https://doi.org/10.1017/s1431927611012074.

Tsai, J.-Y., Pan, J., Lin, H., Bansil, A., and Yan, Q. (2021). Antisite defect qubits in monolayer transition metal dichalcogenides. arXiv, 1–21. arXiv:2105.11019.

Wang, Q.H., Kalantar-Zadeh, K., Kis, A., Coleman, J.N., and Strano, M.S. (2012). Electronics and optoelectronics of two-dimensional transition metal dichalcogenides. Nat. Nanotechnol. 7, 699–712. https://doi.org/10.1038/nnano.2012.193.

Wang, X., Zhang, Y.W., Si, H.N., Zhang, Q.H., Wu, J., Gao, L., Wei, X.F., Sun, Y., Liao, Q.L., Zhang, Z., et al. (2020). Single-atom vacancy defect to trigger high-efficiency hydrogen evolution of MoS₂. J. Am. Chem. Soc. 142, 4298–4308. https://doi.org/10.1021/jacs.9b12113.

Whangbo, M.H., and Canadell, E. (1992). Analogies between the concepts of molecular chemistry and solid-state physics concerning structural instabilities. Electronic origin of the structural modulations in layered transition metal dichalcogenides. J. Am. Chem. Soc. *114*, 9587–9600. https://doi.org/10.1021/ja00050a044.

Yang, H., MacLaren, I., Jones, L., Martinez, G.T., Simson, M., Huth, M., Ryll, H., Soltau, H., Sagawa, R., Kondo, Y., et al. (2017). Electron ptychographic phase imaging of light elements in crystalline materials using Wigner distribution deconvolution. Ultramicroscopy *180*, 173–179. https://doi.org/10.1016/j.ultramic.2017.02.006.

Yang, J., Kawai, H., Wong, C.P.Y., and Goh, K.E.J. (2019a). Electrical doping effect of vacancies on monolayer MoS_2. J. Phys. Chem. C *123*, 2933–2939. https://doi.org/10.1021/acs.jpcc.8b10496.

Yang, J., Wang, Y., Lagos, M.J., Manichev, V., Fullon, R., Song, X., Voiry, D., Chakraborty, S., Zhang, W., Batson, P.E., et al. (2019b). Single atomic vacancy catalysis. ACS Nano *13*, 9958–9964. https://doi.org/10.1021/acsnano.9b05226.

Yu, Y.J., Yang, F.Y., Lu, X.F., Yan, Y.J., Cho, Y.H., Ma, L.G., Niu, X.H., Kim, S., Son, Y.W., Feng, D.L., et al. (2015). Gate-tunable phase transitions in thin flakes of 1T-TaS_2. Nat.

Nanotechnol. *10*, 270–276. https://doi.org/10.1038/nnano.2014.323.

Zhou, J., Lin, J., Huang, X., Zhou, Y., Chen, Y., Xia, J., Wang, H., Xie, Y., Yu, H., Lei, J., et al. (2018). A library of atomically thin metal chalcogenides. Nature *556*, 355–361. https://doi.org/10.1038/s41586-018-0008-3.

Zhou, W., Zou, X., Najmaei, S., Liu, Z., Shi, Y., Kong, J., Lou, J., Ajayan, P.M., Yakobson, B.I., and Idrobo, J.-C. (2013). Intrinsic structural defects in monolayer molybdenum disulfide. Nano Lett. *13*, 2615–2622. https://doi.org/10.1021/nl4007479.

STAR★METHODS

KEY RESOURCES TABLE

REAGENT or RESOURCE	SOURCE	IDENTIFIER
Chemicals, peptides, and recombinant proteins		
KOH	Sigma Aldrich	CAS: 1310-58-3
KI	Sigma Aldrich	CAS: 7681-11-0
Re powder	Sigma Aldrich	CAS: 7440-15-5
Se powder	Sigma Aldrich	CAS: 7782-49-2
PMMA	Sigma Aldrich	CAS: 9011-14-7
Software and algorithms		
Digital Micrograph	Gatan, Inc	https://www.gatan.com
Origin	OriginLab Corporation	https://www.originlab.com
Python	Python Software Foundation	https://www.python.org
VASP 5.5.4	NA	https://www.vasp.at
Other		
Optical microscopy	OLYMPUS Corporation	https://www.olympus-lifescience.com
Electron microscopy	Nion Co.	https://www.nion.com

RESOURCE AVAILABILITY

Lead contact

Further information requests should be directed to the lead contact, Wu Zhou (wuzhou@ucas.ac.cn).

Materials availability

This study did not generate new reagents.

Date and code availability

Data and code used in this paper will be shared by the lead contact upon request. Any additional information required to reanalyze the data reported in this paper are available from the lead contact upon request.

EXPERIMENTAL MODEL AND SUBJECT DETAILS

Our study does not use experimental models typical in the life sciences.

METHOD DETAILS

$ReSe_2$ growth and TEM sample preparation

The monolayer $ReSe_2$ samples were synthesized using a molten-salt-assisted CVD process(Zhou et al., 2018), during which a furnace including a quartz tube was employed. Firstly, 1 mg KI powder and 5 mg Re powder were put together into an aluminum oxide boat. A Si substrate with a surface layer of SiO_2 was placed on the aluminum oxide boat with the smooth surface facing the Re source and with one cm distance. Then the aluminum oxide boat was inserted into the center of the quartz tube. Another boat containing the Se powder was deposited on the upstream of the tube furnace. The furnace was heated with a ramp rate of 50°C min^{-1} to the growth temperature (700-780°C for Re and 300°C for Se) and held for 5 ~ 10 min before cooling down to room temperature naturally. Ar/H_2 with a flow rate of 80/10 sccm was used as the carrier gas.

The TEM samples were prepared with a poly (methyl methacrylate) (PMMA) assisted method. 0.8 μm thick PMMA was spin-coated on the samples deposited on the wafer, and then baked at 180°C for 3 min. After that, the wafer was immersed in the KOH solution (1M) to etch the SiO_2 layer overnight. Afterward, the $ReSe_2$ film was transferred into deionized water several times to wash away the residual contaminants and then fished by a TEM grid. The transferred specimen was dried naturally, and then dropped into

acetone for a whole night to wash away the PMMA coating layers. The TEM sample was baked in the vacuum at 160°C for 8 ∼ 10 hours to reduce the contaminants on the sample before STEM imaging.

Electron microscopy characterization

The STEM-HAADF imaging was conducted on an aberration-corrected Nion U-HERMES100 microscope operating at 60 kV. The probe-forming semi-angle is 32 mrad, and the collection half angle for HAADF imaging is between 75 and 210 mrad. The beam current was about 15 pA for a single shot image with an electron dose rate of ∼ 2000 e⁻/Å²/s. The sequential video was acquired in a multi-frame mode with a relatively low electron dose rate (∼ 180 e⁻/Å²/s) on the same area where a single shot image was just taken. Images used for point defects statistics were processed by removing the effect of the probe tail to more accurately identify the intensity on each atom position(Krivanek et al., 2010). Each frame of the time-sequence video was filtered using a nonlinear filter to increasing the signal to noise ratio(Du, 2015).

The 4D-STEM experiments were performed on the same microscope with the same settings. Since monolayer $ReSe_2$ is very sensitive to electron beam irradiation, the experimental parameters for recording the 4D dataset were optimized after multiple attempts. The beam current, scanning pixel size and exposure time were set to 2 pA, 0.3125 Å and 2 ∼ 4 ms, respectively. The CMOS camera for recording each convergent beam electron diffraction (CBED) has 2048×2048 pixels, which is cropped and binned to 192×192 pixels to reduce the size of the 4D dataset. The CBED bright field disk was centered and the rotation of CBED was corrected by changing the direction of the scanning axis using the shadow image approach(Savitzky et al., 2021). 4D-STEM simulations as well as STEM-HAADF image simulations were implemented on monolayer $ReSe_2$ crystal model containing three types of defects, i.e., V_{Se}, O_{Se} and S_{Se}, using Dr. Probe software(Barthel, 2018). The simulation parameters are set according to experimental conditions. The thermal vibration of the $ReSe_2$ lattice is considered using the frozen phonon method and 30 phonon configurations are employed.

The phase of monolayer $ReSe_2$ is retrieved with our custom-written python codes, using a direct ptychographic method called SSB as has been described in Ref(Pennycook et al., 2015; Rodenburg et al., 1993; Yang et al., 2017). The monolayer characteristic of the sample meets the so-called weak phase object approximation (WPOA) that the SSB method is established on. In addition, the aberration-free condition for the SSB method is also largely satisfied in the experiment through the careful alignment and tuning of the microscope with the aid of the aberration corrector and monochromator.

Density functional calculations

DFT calculations were performed using the Vienna Ab initio Simulation Package (VASP) with the projected augmented wave (PAW) method(Blochl, 1994; Kresse and Furthmuller, 1996). Wave functions were expanded in a plane-wave basis set to 400 eV energy cutoff. Exchange and correlation effects were described using the Perdew-Burke-Ernzerh of generalized gradient approximation(Perdew et al., 1996). All structures are modeled by a supercell with a vacuum layer of 15 Å. Point-defect calculations are performed using 2×2×1 supercells in which the interaction between nearby supercells is negligible because the formation energies of vacancies already converge in this condition (see Figure S11 for details). All atoms are fully relaxed until the net force is less than 0.02 eV Å⁻¹. The Brillouin zone is sampled with a 7 × 7×1 point. Density of states are plotted using the sigma of 0.01.

The formation energy is a function of the chemical potential:

$$E_{form} = E_{defect} - E_{defect-free} + \mu_i - \mu_j$$

where E_{defect} and $E_{defect-free}$ represent the total energies of structure with and without the defect respectively, μ_i is the chemical potential of missing atoms, and μ_j is the chemical potential of substitutional atoms. The formation energy of a Se vacancy is $E(V_{Se}) = E_{defect} - E_{defect-free} + \mu_{Se}$, while the formation energy of an antisite defect at Se site (Re_{Se}) is $E(Re_{Se}) = E_{defect} - E_{defect-free} + \mu_{Se} - \mu_{Re}$, and the formation energy of an antisite defect at Re site is $E(Se_{Re}) = E_{defect} - E_{defect-free} + \mu_{Re} - \mu_{Se}$. For Se-rich conditions, μ_{Se} is the energy of a Se atom in Se8 molecules. For Se-poor conditions, μ_{Se} is $[E(ReSe_2)-E(Re_{bulk})]/2$ which corresponds to Re atoms in bulk form.

QUANTIFICATION AND STATISTICAL ANALYSIS

Values shown in Figure 3D are obtained by calculating the concentration of each type of point defects based on a large number of STEM-HAADF images. Error bars in Figure 3D are the standard deviations of the concentrations of each type of point defects. Curves in Figures 5E and 5F are obtained by calculating the number of vacancies in Figures 5A–5D.